Journal of Advanced Ceramics
先进陶瓷
ISSN 2226-4108
CN 10-1154/TQ
清华大学出版社 Tsinghua University Press
SciOpen

J Adv Ceram 2026, **15**: 9221322

https://doi.org/10.26599/JAC.2026.9221322

Research Article

Ultrafast low-temperature fabrication of strong and tough high-entropy borides-based ceramics via reactive $ZrSi_2$-assisted heavy direct current sintering

Lehao Liu[a], Yingjun Liu [a, b, *], Yuhan Yaoa, Yufei Zu[c,*], Zhaofu Zhang[d], Jianjun Sha[e], Yang Zhang[a, b], Hongfeng Dong[a, b], Nan Zhang[a, b], Shujing Zhang[a], Ning Zhang[a], Wenhao Yue[a], Yibo Zhang[a], Wuhao Cao[a], Yuan Hu[a], Ruiheng An[a], Wenhu Li[a, b, *], Luyi Zhu[f, *], Taotao Ai [a, b, *]

[a] *School of Materials Science and Engineering, Shaanxi University of Technology, Hanzhong 723001, China.*

[b] *National and Local Joint Engineering Laboratory for Slag Comprehensive Utilization and Environmental Technology, School of Materials Science and Engineering, Shaanxi University of Technology, Hanzhong 723001, China.*

[c] *School of Materials Science and Engineering, Dalian University of Technology, Dalian 116024, China.*

[d] *Xi'an Aerospace Composites Research Institute, Xi'an 710025, China.*

[e] *State Key Laboratory of Structural Analysis, Optimization and CAE Software for Industrial Equipment, Dalian University of Technology, Dalian 116024, China.*

[f] *State Key Laboratory of Crystal Materials, Institute of Crystal Materials, Shandong University, Jinan 250100, China.*

* Corresponding authors.

E-mail: Y. Liu, yjliu@snut.edu.cn;

Y. Zu, yfzu@dlut.edu.cn;

W. Li, ccwhli@163.com;

L. Zhu, zhuly@sdu.edu.cn;

T. Ai, aitaotao0116@126.com

Received: January 30, 2026; Revised: May 13, 2026; Accepted: May 18, 2026

Abstract: The ultra-high sintering temperatures required for high-entropy borides (HEB) pose a significant challenge to their processing and practical application. This study introduces an efficient low-temperature fabrication route for dense HEB-based ceramics using reactive $ZrSi_2$-assisted heavy direct current sintering, with a maximum heating rate exceeding 3700 °C/min. A porosity of 1.60 ± 0.61% can be achieved at a sintering temperature of 1000 °C, which is reduced by 600-1000 °C compared to state-of-the-art spark plasma sintering/field-assisted sintering techniques processing of HEBs. Microstructural analysis revealed interdiffusion between HEB and $ZrSi_2$, leading to a core-shell HEB architecture and layered high-entropy silicides. Meanwhile, dislocations and non-uniform stress fields were observed within the HEB grains. These microstructural features synergistically inhibit crack propagation and promote crack deflection and branching. Consequently, both flexural strength and fracture toughness are significantly enhanced. A flexural strength of 963 MPa was attained at 1400 °C, and a fracture toughness of 7.4 $MPa \cdot m^{1/2}$ was achieved at 1500 °C, surpassing most reported HEB-based ceramics. These results demonstrate that reactive $ZrSi_2$-assisted heavy direct current sintering is a profoundly effective approach for low-temperature manufacturing of high-performance HEB-based ceramics.

Keywords: high-entropy borides; ultrafast sintering; low temperature densification; core-shell structure; mechanical properties

1. Introduction

High-entropy borides (HEBs), particularly those based on transition metals, have attracted considerable interest due to their exceptional combination of ultra-high melting points, excellent mechanical properties, and superior oxidation resistance [1]. These characteristics make them highly promising for extreme-temperature applications [2-4]. However, the widespread adoption of these materials is hindered by two intrinsic and interrelated limitations: inherent brittleness and formidable sintering challenges [5, 6]. The robust covalent and mixed ionic bonding in HEBs contributes to their high hardness but often leads to low fracture toughness, typically ranging from 2 to 4 $MPa \cdot m^{1/2}$, thereby substantially constraining their resistance to damage [7]. Moreover, the attainment of full densification of HEBs conventionally necessitates extended thermal treatment at temperatures exceeding 2000 °C [8-10]. Such high-temperature, long-duration processing often results in pronounced grain coarsening, which is detrimental to mechanical properties.

To address these challenges, considerable research efforts have been concentrated along two primary avenues. The first approach emphasizes advanced field-assisted sintering techniques (FAST), such as spark plasma sintering (SPS), which employs external pressure combined with pulsed direct current to enhance densification kinetics. Recent studies have further elucidated the densification mechanisms during SPS; for instance, Smith et al. identified grain boundary diffusion as the dominant mechanism for $(TiZrNbHfTa)B_2$ with an activation energy of 575 kJ/mol [11]. Alternative sintering routes, such as self-propagating high-temperature synthesis combined with SPS (SHS-SPS), have also been successfully employed to fabricate dual-phase high-entropy carbide-boride (HEC-HEB) ceramics at 1800 °C, achieving a fracture toughness of 5.6 $MPa \cdot m^{1/2}$ [12]. Moreover, the introduction of metallic sintering aids like Ta has been shown to significantly promote densification, reducing open porosity to as low as 0.15% [13]. Although effective, the densification of HEB via FAST/SPS still typically requires temperatures above 1800-2000 °C [8, 11-17]. The second approach centers on composite design through the incorporation of reinforcing phases such as fibers, whiskers, or secondary ceramic

particles (e.g., SiC, B_4C) to promote crack deflection and improve toughness [9, 14, 16, 18]. Novel toughening strategies, including the incorporation of secondary phases such as Al_2O_3 [19], Ti_3AlC_2 [20], have been explored to overcome the inherent brittleness of HEBs. On the other hand, the in-situ formation of nanocomposites via polymer-derived ceramic routes has enabled precise control over microstructural features [21, 22]. While these strategies offer improvements, they often entail complex multi-step processing, high costs, and fail to resolve the trade-off between densification and fine-grained microstructure retention.

Herein, we propose an integrated synthesis-sintering strategy that simultaneously addresses these challenges. Our approach utilizes an in-situ reactive precursor, $ZrSi_2$, within a high-entropy diboride matrix processed by heavy direct current-assisted sintering. This strategy is founded on two principles. First, from a thermodynamic perspective, $ZrSi_2$ is designed to react with the boride matrix during sintering, in-situ generating well-dispersed reinforcing phases. This reaction is thermodynamically favorable and promotes strong matrix-reinforcement interfaces [23]. Second, from a processing viewpoint, the metallic nature of $ZrSi_2$ ensures good electrical conductivity, making it highly compatible with the direct current-assisted sintering [24]. The conductive precursor facilitates effective Joule heating and rapid densification, aligning with emerging ultrafast sintering paradigms.

Despite the proven effectiveness of in-situ formation techniques in other ceramic systems, their application for tailoring microstructural features such as core-shell architectures in high-entropy ceramic composites remains largely unexplored [25, 26]. In particular, there is a limited fundamental understanding regarding the microstructural evolution, particularly the formation of unique architectures like core-shell structures, through in-situ reactions within high-entropy systems. More critically, the synergistic strengthening and toughening mechanisms imparted by such in-situ generated structures have yet to be explored.

Therefore, this work presents a methodology for fabricating a novel core-shell structured high-entropy borides composite via heavy direct current-assisted sintering using $ZrSi_2$ as a reactive

precursor. Exceptional densification was achieved at extremely low temperatures (as low as 1000 °C) and ultra-high heating rates (average heating rates exceeding 1600 °C/min), with sintering temperatures reduced by 600-1000 °C compared to state-of-the-art SPS/FAST processing of HEBs [8, 11-17]. A uniformly distributed core-shell high-entropy boride was formed. Furthermore, the strengthening and toughening mechanisms of resulting microstructures were investigated. This study establishes a novel and energy-efficient paradigm that bypasses the traditional densification-mechanical properties dilemma, paving the way for high-performance, damage-tolerant ultra-high temperature ceramics.

2. Experimental procedure

2.1. Powder preparation and sintering

$(Ti_{0.2}Zr_{0.2}Nb_{0.2}Hf_{0.2}Ta_{0.2})B_2$ (HEB) powder synthesized by boron thermal reduction [27] and commercial $ZrSi_2$ powder (purity >99%, particle size 2-5 μm, Shanghai Macklin Biochemical Co., Ltd) were used as starting materials. The powders were mixed in a composition of 80 vol% HEB and 20 vol% $ZrSi_2$. This ratio was selected based on prior studies on ZrB_2-$ZrSi_2$ systems, where 20 vol% $ZrSi_2$ was found to effectively promote densification while preserving a high fraction of the boride phase [28]. The powder mixture was ball-milled in ethanol for 36 hours using WC milling media. The resulting slurry was vacuum-dried and sieved.

Densification of the HEB-$ZrSi_2$ powders was performed using a direct current field-assisted sintering furnace (6000 A, 12 V). To improve heating efficiency, sintering was conducted in an improved multilayer mold as described in our previous work [29]. The sintering mold consisted of an inner graphite liner, a boron nitride (BN) insulating interlayer, and an external graphite die. A pressure of 50 MPa was applied and maintained throughout the process. A heavy constant direct current with a current density of 1250 A/cm^2 was used for rapid heating. The heavy direct current assisted sintering used in this work differs from conventional SPS in several key aspects: (i) continuous direct current (no pulsing) with higher current density; (ii) ultrafast heating rates achieved through the multilayer

mold. Unlike flash sintering (FS), which relies on an abrupt thermal runaway event, our process maintains controlled heating throughout the cycle. Upon reaching the target temperature, the current was manually regulated to maintain that temperature for 3 min. Sample temperature was monitored using a two-color infrared thermometer (STRONG-SR-7025WL, Changzhou Sijie Optoelectronics Technology Co. Ltd., China), with the measurement point positioned approximately 2 mm from the sample. The resulting ceramics sintered at 1000, 1200, 1300, 1400 and 1500 °C were labeled as HZ1000, HZ1200, HZ1300, HZ1400 and HZ1500, respectively. All sintering runs employed identical molds and nominally equivalent powder quantities. Real-time displacement monitoring was used to analyze densification behavior, with displacement data calibrated against blank reference samples.

2.2. Characterization

The oxygen content of powders was detected by an oxygen analyzer (ONH836, LECO, USA). The bulk density of sintered samples was measured by the Archimedes' method using deionized water. Porosity was evaluated from the pore area fraction in SEM images, using ImageJ software. The phase content in the sintered samples was analyzed using the same method. For each sample, at least 10 randomly selected SEM images were analyzed. For core dimensions and shell thickness, statistical analysis was performed using BSE images.

Phase identification was performed by X-ray diffraction (XRD, Rigaku SmartLab) over a 2θ range of 20° to 80° with a step size of 0.01° and a scanning speed of 1°/min. Microstructural characterization was carried out using scanning electron microscopy (SEM, JEOL 7610F Plus) equipped with a back-scattered electron (BSE) detector. Elemental analysis was conducted via energy-dispersive X-ray spectroscopy (EDS, Ultim Extreme). Nanoscale structural and chemical analysis was performed using field-emission transmission electron microscopy (Talos F200XG2) and spherical aberration correction transmission electron microscope (Titan Cubed Themis G2 300). TEM samples were prepared via focused ion beam milling (TESCAN AMBER GMH).

Flexural strength was determined by the three-point bending test on bars (cross-sectional

dimensions of 2 mm high × 2.5 mm wide) with a span of 20 mm and a crosshead speed of 0.5 mm/min. Fracture toughness was evaluated using the single-edge notched beam (SENB) method on bars (cross-sectional dimensions of 4 mm high × 2 mm wide) with a notch depth of 2 mm and a notch width of <0.3 mm. The supporting span was 16 mm, and a crosshead speed of 0.05 mm/min was used. Fracture toughness (K_{IC}) was calculated using Eqs. 1-2 as specified in ASTM C1421. At least three specimens were tested for each condition. To examine the crack extension characteristics, a selected sample was indented with a load of 10 kgf. The crack propagation paths were examined by SEM.

$$K_{IC} = \mathrm{g}\left[\frac{PL \times 10^{-6}}{BH^{1.5}}\right]\left[\frac{1.5[a/H]^{0.5}}{[1-a/H]^{1.5}}\right] \quad (1)$$

$$g = \frac{1.99 - [a/H][1-[a/H]][2.15 - 3.93[a/H] + 2.7[a/H]^2]}{1 + 2[a/H]} \quad (2)$$

Where B (m) and H (m) are the width and thickness of the test specimen, P (N) the maximum load value, L (m) the span, a (m) the notch depth of the test specimen, and g the shape factor.

3. Results and discussion

3.1. Densification and microstructure

To understand the densification behavior, the shrinkage curves during reactive $ZrSi_2$-assisted heavy direct current sintering were first monitored. Fig. 1(a) shows the sintering curve for HEB ceramic under a load of 50 MPa with temperature up to 1500 °C. An enlarged pattern shows ultrafast heating stage (Fig. 1(b)). Densification behavior is reflected in differential displacement versus sintering temperature curve, with the temperature differential curve also presented. Shrinkage commenced at approximately 815 °C, with maximum shrinkage occurring at 956 °C. The shrinkage rate approaches zero during the holding period, indicating near-complete densification. Notably, the maximum heating rate reached 3750 °C/min, with an average heating rate of 1674 °C/min, significantly exceeding conventional sintering rates and implying shorter cycles and lower energy consumption. The maximum heating rate was achieved during the initial stage of sintering, where the

electrical resistivity of the powder compact is highest, leading to significant Joule heating. This ultra-high initial heating rate promotes rapid particle surface activation and enhances grain boundary diffusion while suppressing surface diffusion and grain coarsening [30, 31], thereby contributing to the low-temperature densification observed in this study. Furthermore, the total sintering cycle time (including the heating and holding stages) was less than 4 min for the 1500 °C run, compared to typical SPS cycles for HEB ceramics that often exceed 20 min [8, 11-17], demonstrating the energy-efficient nature of this approach. Based on the shrinkage curves, sintering processes were conducted at 1000 °C, 1200 °C, 1300 °C, 1400 °C.

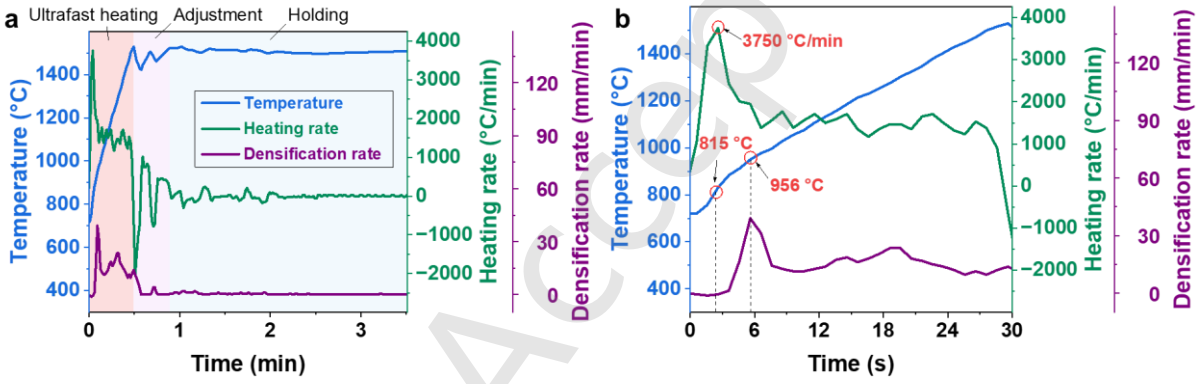

Fig. 1 (a) Sintering curve of HEB-based ceramic via reactive $ZrSi_2$-assisted heavy direct current sintering and (b) enlarged pattern showing ultrafast heating stage.

SEM and BSE images in Figs. 2(a)-2(h) illustrate the microstructural evolution of as-sintered samples. No significant visible pores are observed in all samples, indicating the achievement of high-density materials. Based on graphical analysis, the porosity of the as-sintered samples was evaluated from the pore area fraction in SEM images (Figs. 2(i)-2(j)), with the results summarized in Fig. 2(k). The porosity of sample sintered at 1000 °C is 1.60 ± 0.61%. As the sintering temperature increases to 1400 °C, the porosity of sample decreases to 0.91±0.19%. At 1500 °C, the porosity slightly increases to 1.81 ± 0.48%, which might be attributed to minor grain coarsening or coalescence of closed pores (Fig. 2(h)). Overall, the porosity of all samples remains below 3 %, demonstrating that highly dense

HEB-based ceramics can be produced at temperatures as low as 1000 °C.

Accurate temperature calibration remains a persistent challenge in ultrafast sintering. For SPS-sintered ZrB_2 ceramics, finite element simulations reveal a temperature difference of approximately 20 °C between the sample and a point 2 mm away, while the temperature gradient between the surface and core of a 30 mm-diameter sample reaches about 100 °C [32]. In ultrafast high-temperature sintering (UHS) using carbon felt as the heating element, the temperature difference between the surface and core of an 8 mm-diameter sample is reported to be less than 100 °C at heating rates of 2600-2900 °C/min [33]. For UHS of ZrB_2-B_4C composites heated to 2512 °C within 10 s, theoretical simulations indicate that after a 60 s hold, the temperature of the carbon felt exceeds that of the sample by less than 300 °C [34]. In practice, owing to strong thermal radiation from the surface, the measured temperature of the carbon felt is lower than the actual internal temperature of the sample. To establish accurate temperature calibration for the sample environment, high-purity Ni, Pt, Nb, and single-crystal alumina have been employed as melting point standards, revealing that the sample temperature is < 260 °C higher than the surface temperature of the carbon felt [35]. When using graphite powder as the heating element at a heating rate of 500 °C/min for a 30 mm-diameter sample, the surface-to-core temperature difference is less than 450 °C with no holding time and reduces to less than 20 °C after a 180 s hold [36]. In modified SPS-UHS, where thin-walled graphite replaces carbon felt and graphite powder as the heating element, a 20 mm-diameter sample is placed within a 50-mm-diameter, 3-mm-thick graphite heating element for pressureless sintering. At a heating rate of 3600 °C/min, simulations show that the maximum temperature of the heating element reaches approximately 2000 °C, which is about 400 °C higher than that of the sample [37]. In our work, a thin-walled graphite heating element is similarly employed to achieve rapid heating. Given the close contact between the sample and the die, which facilitates efficient heat transfer, and the relatively short distance of 2 mm between the temperature measurement point and the sample, the temperature difference between the measured temperature and the actual sample temperature is likely less than 400 °C. This difference is expected

to further decrease during the subsequent 3 min holding period. Consequently, the densification temperature in this work is likely below 1400 °C. This is considerably lower than the values typically reported for HEB-based ceramics, which often exceed 1800 °C [8, 14-17].

For the microstructures shown in Figs. 2(a)-2(h), a gray phase surrounds a grayish-white phase, forming a core-shell structure. As the sintering temperature increases, the shell thickness grows, accompanied by grain growth. The mean grain size of the core and thickness of the shell were evaluated by SEM images. The results are summarized in Table 1. Specifically, the mean grain size of the core remained within the range of 300-330 nm. Meanwhile, the thickness of the shell increased from 80 ± 47 nm to 239 ± 188 nm. This indicates that matrix grain growth was primarily associated with shell growth. Core-shell particles are uniformly dispersed within the samples. In addition to matrix core and shell phases, black and white phases are also observed. The findings suggest that the phase composition of HEB-based ceramics evolves as the temperature increases from 1000 °C to 1500 °C.

XRD analysis was performed with Si powder coated on the sample surface as an internal standard for peak-position calibration. Results are summarized in Fig. 3. Fig. 3(a) shows the evolution from the initial mixed HEB and $ZrSi_2$ powders to the sintered products. In the mixed powder, diffraction peaks corresponding to $ZrSi_2$ (PDF#97-001-6772) and HEB are clearly visible. After high-temperature sintering, $ZrSi_2$ diffraction peaks diminish and eventually disappear, while peaks corresponding to two new silicide phases emerge. One is a tetragonal silicide, similar to $(Ta_{0.2}W_{0.8})Si_2$ (PDF#97-065-2346), and the other is a hexagonal silicide. A full-spectrum fit was performed on the XRD pattern (Fig. 3(b)), revealing that the lattice parameters of the hexagonal silicide in HT1500 are a = 4.74 Å and c = 6.54 Å, resembling the hexagonal $(TiNbMoTaW)Si_2$ with lattice parameters of a = 4.71 Å and c = 6.52 Å reported by Gild et al. [38]. The formation of the new silicides may be due to the diffusion of elements from HEB into $ZrSi_2$. In addition, trace amounts of SiC and $(Hf,Zr)O_2$ were also detected. The SiC may originate from the reaction between $ZrSi_2$ and WC, with about 2 vol% WC introduced during the ball-milling process. There are two sources of $(Hf,Zr)O_2$: (i) the synthesis of HEB powder, in which

the oxygen analyzer detected an oxygen content of 0.57 wt%; (ii) slight oxidation occurring during the ball milling, drying, and sieving of the mixed HEB-$ZrSi_2$ powder. These oxidation products may exist in an amorphous state but can crystallize after high temperature sintering [39].

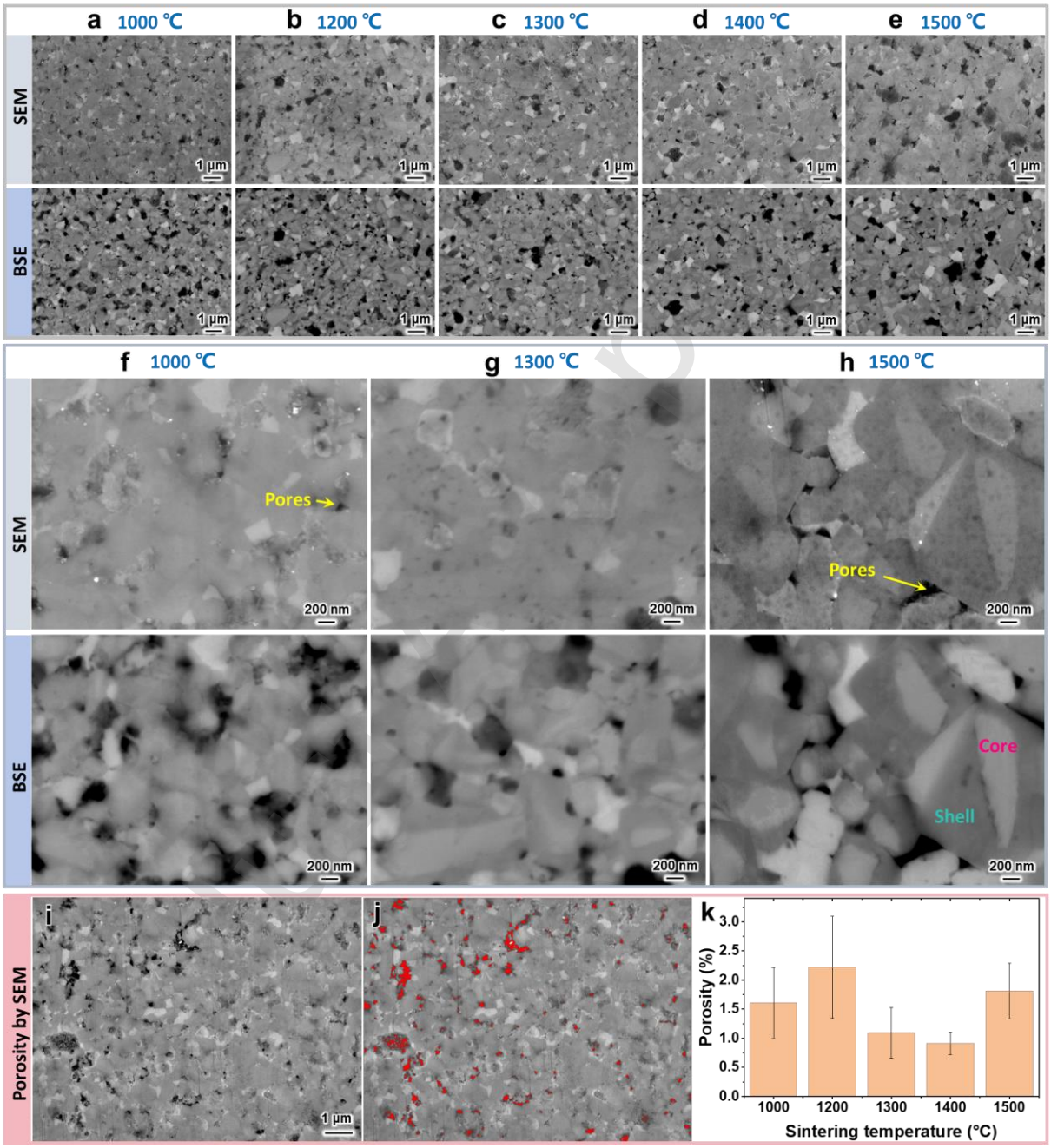

Fig. 2 SEM image of polished surface of HEB-based ceramics sintered at different temperatures: (a) 1000 °C, (b) 1200 °C, (c) 1300 °C, (d) 1400 °C, (e) 1500 °C; High-magnification SEM images: (f) 1000 °C, (g) 1300 °C, (h) 1500 °C. Porosity evaluated from the pore area fraction in SEM images: (i)

SEM images of HZ1000 and (j) the pore regions marked in red, (k) summarized statistical results of the porosity of sintered samples.

Table 1 Density, porosity and phase content of as-sintered samples.

	HZ1000	HZ1200	HZ1300	1400	1500
Density (g/cm^3)	7.34	7.50	7.53	7.58	7.57
Porosity (vol%)	1.60 ± 0.61	2.22 ± 0.88	1.09 ± 0.44	0.91 ± 0.19	1.81 ± 0.48
Grain size of HEB core (nm)	306 ± 132	312 ± 178	319 ± 155	329 ± 136	319 ± 150
Thickness of HEB shell (nm)	80 ± 47	125 ± 65	167 ± 144	199 ± 119	239 ± 188
HEB core (vol%)	52.28 ± 5.12	34.55 ± 4.55	29.93 ± 4.27	23.23 ± 3.54	11.41 ± 2.36
HEB shell (vol%)	21.03 ± 2.23	41.18 ± 4.46	47.05 ± 3.89	55.12 ± 5.11	67.11 ± 5.78
Silicides (vol%)	19.96 ± 2.22	15.63 ± 1.88	14.97 ± 1.93	13.27 ± 3.50	12.46 ± 1.44
(Hf,Zr)O_2 (vol%)	3.21 ± 0.51	3.79 ± 0.72	3.85 ± 0.87	3.85 ± 1.37	3.47 ± 0.82
SiC, SiO_2 (vol%)	1.91	2.63	3.11	3.61	3.74

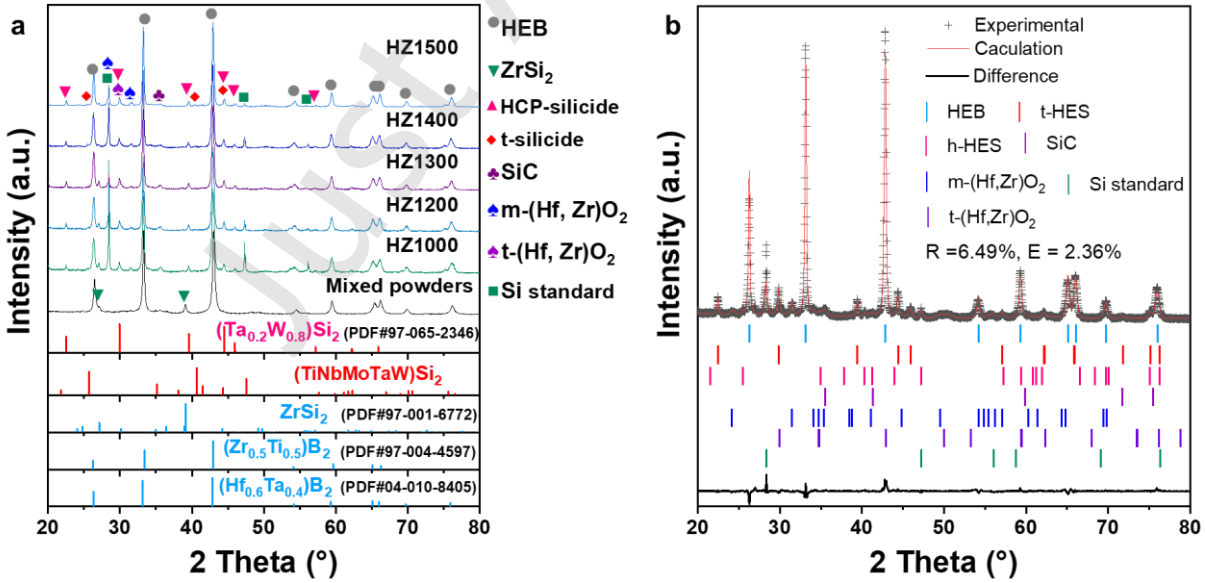

Fig.3 (a) XRD patterns of HEB-based ceramics, (b) Rietveld full spectrum fitting diagrams of HZ1500.

Fig. 4 presents a comprehensive analysis of the sample sintered at 1400 °C (HZ1400). The BSE image (Fig. 4(a)) reveals five phases with white, grayish-white, gray, dark gray, and black contrast. EDS spot analysis was performed on these phases. The results are presented in Figs. 4(b)-4(h) and Table 2. EDS line scans across core-shell structures are shown in Figs. 4(i)-4(j). The core-shell structure consists of a gray-white core surrounded by a gray shell, both identified as high-entropy borides. The shell exhibits higher Zr content and lower Hf content compared to the core (Table 2). Elemental concentration profiles across the core-shell region (Figs. 4(i)-4(j)) show a distinct increase in Zr and decreases in Hf and Ta from core to shell. Additional phases were also identified: a gray-black phase containing O, Si, Ti, Zr, and Hf elements; a black phase containing C, Si, Ti, and Hf elements (Figs. 4 (a), 4(g), and 4(h)). Two species were detected in the white phase: one with smooth, regular grain boundaries is (Hf, Zr)O_2, and the other is a silicide containing Si, Nb, Ta, Ti, and W elements (Figs. 4(a), 4(d) and 4(f)). Although tetragonal and hexagonal silicides were detected by XRD, distinguishing between the two phases using SEM-BSE-EDS proved challenging. As shown in high-magnification SEM image (Fig. 4(k)), these silicides exhibit a layered structure. The volume fractions of individual phases were evaluated from SEM/BSE images, with the results summarized in Table 1. With increasing sintering temperature, the volume fraction of the HEB core decreased from 52.28 ± 5.12% to 11.41 ± 2.36%, whereas that of the HEB shell increased from 21.03 ± 2.23% to 67.11 ± 5.78%. Meanwhile, the volume fraction of silicides decreased from 19.96 ± 2.22% to 12.46 ± 1.44%, while the volume fraction of (Hf,Zr)O_2 remained relatively stable, ranging between 3.2% and 3.9%. The decrease in silicide volume fraction with increasing sintering temperature may be due to density change of the silicide phase and redistribution of Si into secondary phases.

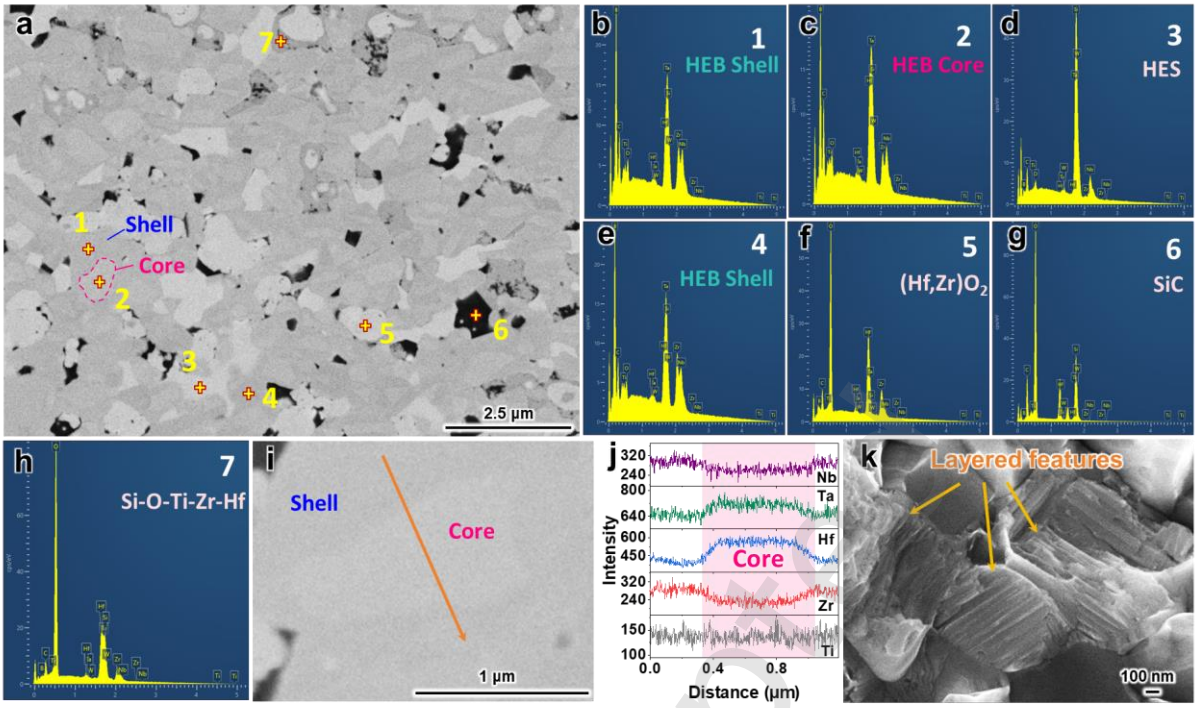

Fig. 4 (a) BSE image of the 1400 °C-sintered sample, (b-h) EDS spot analysis, (i-j) EDS line analysis of high-entropy boride core-shell structures, (k) high-magnification SEM image revealing the layered structure of the silicide.

Table 2 Summary of EDS spot analysis results for the selected region marked in Fig .4(a).

Element	Content (at.%)						
	1 (HEB Shell)	2 (HEB Core)	3 (HES)	4 (HEB Shell)	5 ($(Hf,Zr)O_2$)	6 (SiC)	7 (Si-O-Ti-Zr-Hf)
B	64.55	60.63	7.15	65.48	8.3	0	5.43
C	12.57	16.7	18.94	10.56	14.66	23.7	9.66
O	1.6	1.73	2.15	1.55	49.57	43.18	55.82
Si	0	0	46.46	0	0	25.24	12.54
Ti	4.64	3.96	1.07	5.21	1.92	6.7	2.88
Zr	5.62	3.91	0.08	6.63	11.54	0	5.38
Nb	4.25	4.49	10.34	4.07	0	0	0
Hf	2.37	3.63	0.08	2.11	13.03	1.18	7.95
Ta	4.36	4.42	4.89	4.36	0.81	0	0.33
W	0.05	0.54	8.83	0.04	0.16	0	0

Note: EDS quantification of light elements (B, C, O) in multiphase ceramics is subject to significant uncertainty. The reported values are considered semi-quantitative, particularly for B and C.

TEM analysis was performed to identify crystal structures and compositions. Fig. 5(a) shows a

TEM image of HZ1400 after cutting and thinning via focused ion beam milling (FIB) technique. Corresponding EDS mappings (Fig. 5(b)) distinguish boride and silicide regions. Within boride grains, elemental concentration variations are identifiable: Zr and Ti are enriched near grain shell, while Hf predominates in the grain cores. In the silicide regions, in addition to Si element, elements such as Nb, Ta, and W were also clearly observed. These results suggest elemental interdiffusion occurred during sintering. Selected area electron diffraction (SAED) patterns confirm that both core and shell regions of the boride belong to the hexagonal system, with core and shell lattice constants a, c being 3.09, 3.34 Å and 3.11, 3.40 Å, respectively (Fig. 5(c) and 5(d)). The HEB shell enriched in Zr exhibits a slightly larger lattice constant, while the HEB core depleted in Zr possesses a slightly smaller one (Table 3), owing to the relatively large atomic radius of Zr atoms.

Notably, the SAED pattern of the silicide does not match orthorhombic $ZrSi_2$ (Fig. 5(e)). Instead, it corresponds to the $[\bar{1}01]$ zone axis of a hexagonal crystal lattice with a space group of P622. Based on EDS analysis (Table 2), the silicide phase contains Ti, Nb, Ta and W in an atomic ratio of Ti:Nb:Ta:W = 0.04:0.41:0.20:0.35, with (Ti + Nb + Ta + W):Si≈1:1.85. Thus, the nominal formula of the silicide phase can be expressed as $(Ti_{0.04}Nb_{0.41}Ta_{0.20}W_{0.35})Si_{1.85}$. This Si:metal ratio deviates from the ideal 2:1 stoichiometry of typical disilicides, suggesting the possible presence of point defects or a non-stoichiometry. Considering the atomic ratio and SAED pattern, the silicide phase is assumed to be $(Ti_{0.04}Nb_{0.41}Ta_{0.20}W_{0.35})Si_2$, with lattice parameters a=4.75 Å and c= 6.51 Å. Notably, previous studies on high-entropy silicides have demonstrated that hexagonal structures are achievable in multi-component systems. For instance, $(TiVNbMoW)Si_2$ [40], $(VNbCrMoW)Si_2$ [41], $(TiZrNbMoW)Si_2$ [42], $(TiNbMoTaW)Si_2$ [38] and $(Ti_{0.22}Zr_{0.06}Nb_{0.28}Mo_{0.22}W_{0.22})Si_2$ [43] all crystallize in hexagonal structures with lattice parameters of a = 4.65-4.73 Å, c = 6.48-6.56 Å, as shown in Table 3. Our lattice parameters (a = 4.75 Å, c = 6.51 Å) are similar to the aforementioned results, which supports the identification of the hexagonal crystal system.

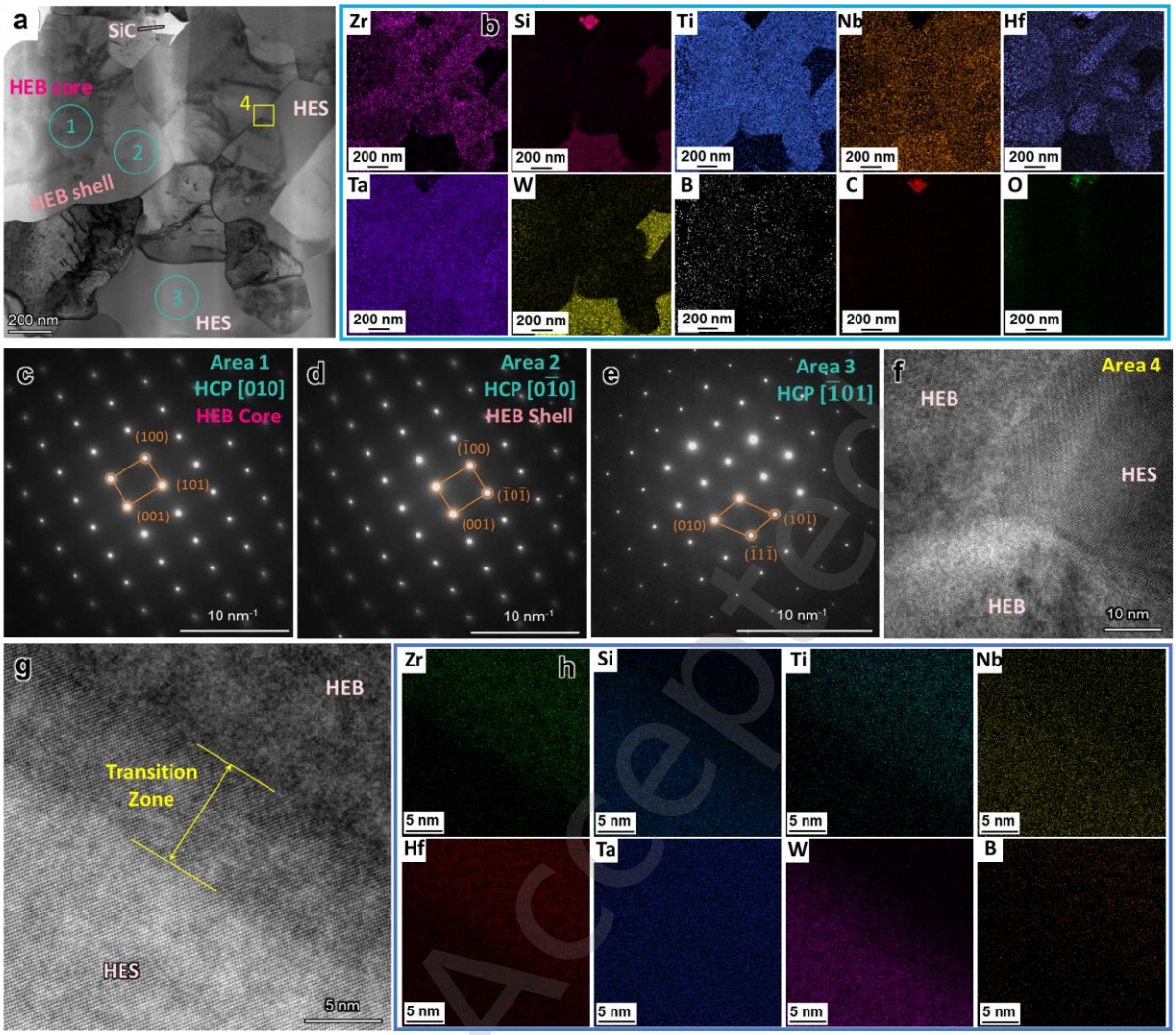

Fig. 5 TEM analyses: (a) morphological images of HZ1400 and (b) EDS mappings; (c-e) SAED patterns of area 1, 2 and 3 marked in (a); (f) HRTEM of area 4 marked in (a), (g) HRTEM of HEB-HES interface and (h) EDS mappings.

Table 3 Lattice parameters of hexagonal borides and hexagonal silicides [38, 40-44].

Composition	a (Å)	c (Å)
$(TiZrNbHfTa)B_2$ (core)	3.09	3.34
$(TiZrNbHfTa)B_2$ (shell)	3.11	3.40
$(TiZrNbHfTa)B_2$	3.11	3.37
TiB_2	3.03	3.22
ZrB_2	3.17	3.54

NbB_2	3.11	3.32
HfB_2	3.14	3.49
TaB_2	3.10	3.33
$(Ti_{0.04}Nb_{0.41}Ta_{0.19}W_{0.35})Si_2$	4.75	6.51
$(TiVNbMoW)Si_2$	4.67	6.48
$(VNbCrMoW)Si_2$	4.69	6.51
$(TiZrNbMoW)Si_2$	4.65	6.51
$(TiNbMoTaW)Si_2$	4.71	6.52
$(Ti_{0.22}Zr_{0.06}Nb_{0.28}Mo_{0.22}W_{0.22})Si_2$	4.73	6.56
$NbSi_2$	4.81	6.59
$TaSi_2$	4.78	6.55
WSi_2	4.62	6.65

High-resolution TEM (HRTEM) reveals a transition zone with a width of ~7.4 nm between HEB and the newly formed high-entropy silicide (HES) (Fig. 5(f) and 5(g)). Elemental distribution across the HEB-HES interface (Fig. 5(h)) shows gradual intensity variations within the transition zone. To further clarify compositions, atomically resolved STEM images and EDS mappings were acquired using spherical-aberration-corrected TEM. Fig. 6(a) and 6(b) show the HAADF-STEM image and EDS mappings of HEB and hexagonal $(Ti_{0.04}Nb_{0.41}Ta_{0.20}W_{0.35})Si_2$. The results indicate that both HEB and hexagonal $(Ti_{0.04}Nb_{0.41}Ta_{0.20}W_{0.35})Si_2$ exhibit non-homogeneous atomic-level distributions for both transition metal and nonmetal elements.

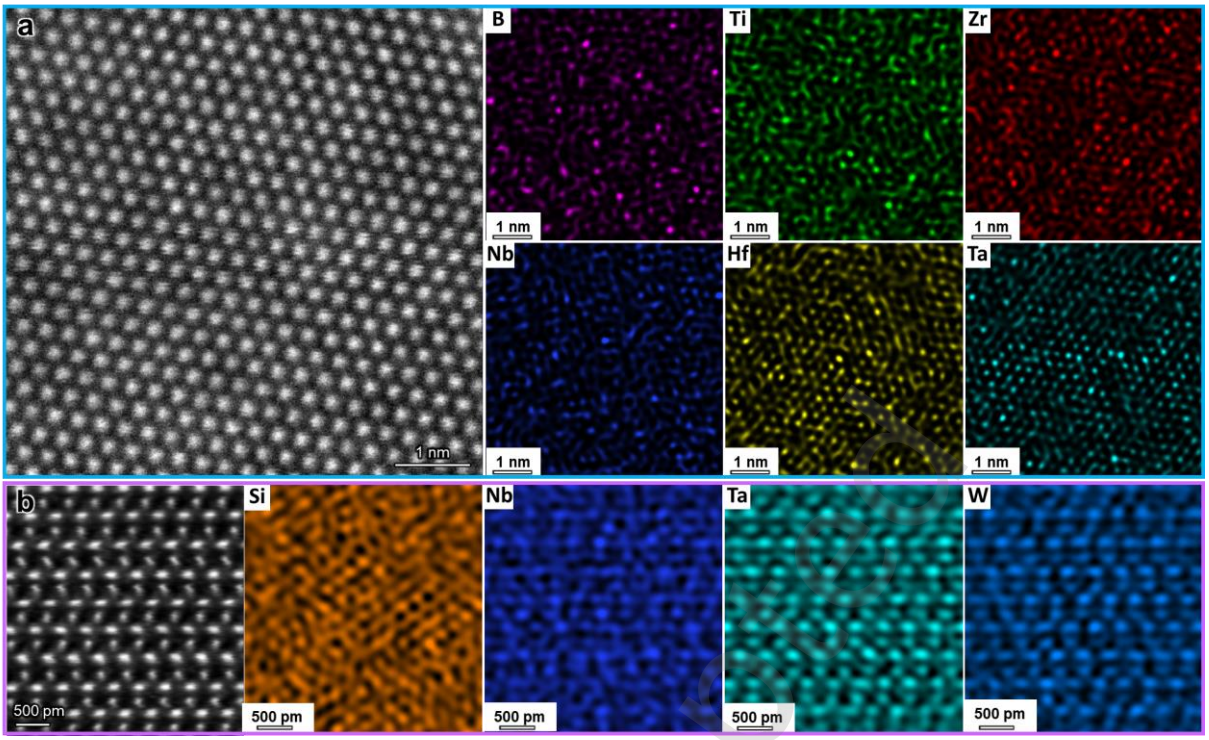

Fig.6 HAADF-STEM image of (a) HEB and (b) hexagonal $(Ti_{0.04}Nb_{0.41}Ta_{0.19}W_{0.35})Si_2$ and the corresponding atomically resolved EDS mappings.

Furthermore, in addition to the HEB core and HEB shell, $(Hf,Zr)O_2$ and SiC were identified (Fig. 7(a)). Tetragonal HES was also identified (Fig. 7(b)). These findings are consistent with the XRD results. EDS spot analysis revealed no statistically significant compositional difference between the tetragonal HES and the hexagonal HES. Regions rich in Si and O were identified in Fig. 7(a), and their morphological characteristics were shown in Figs. 7(c) and 7(d). Fig. 7(e) summarizes EDS spot analysis of selected area in Fig. 7(c). The bright white phase in Fig. 7(c) corresponds to HES. In Fig. 7(d), SiC and Si-O-C-Ta-Hf phases are distributed within the large gray SiO_2 matrix. The formation of SiC can be attributed to the reaction products of WC and $ZrSi_2$. Low-melting-point oxides can form a transitional liquid phase at high temperatures [45]. The ultrafast sintering process allows liquid phases to persist for a limited time, thereby promoting material densification [46]. In summary, the ultrafast low-temperature densification of HEB-based ceramics in this work is likely attributed to elemental interdiffusion between the silicides and the HEB matrix, as well as the ultrafast heating rate.

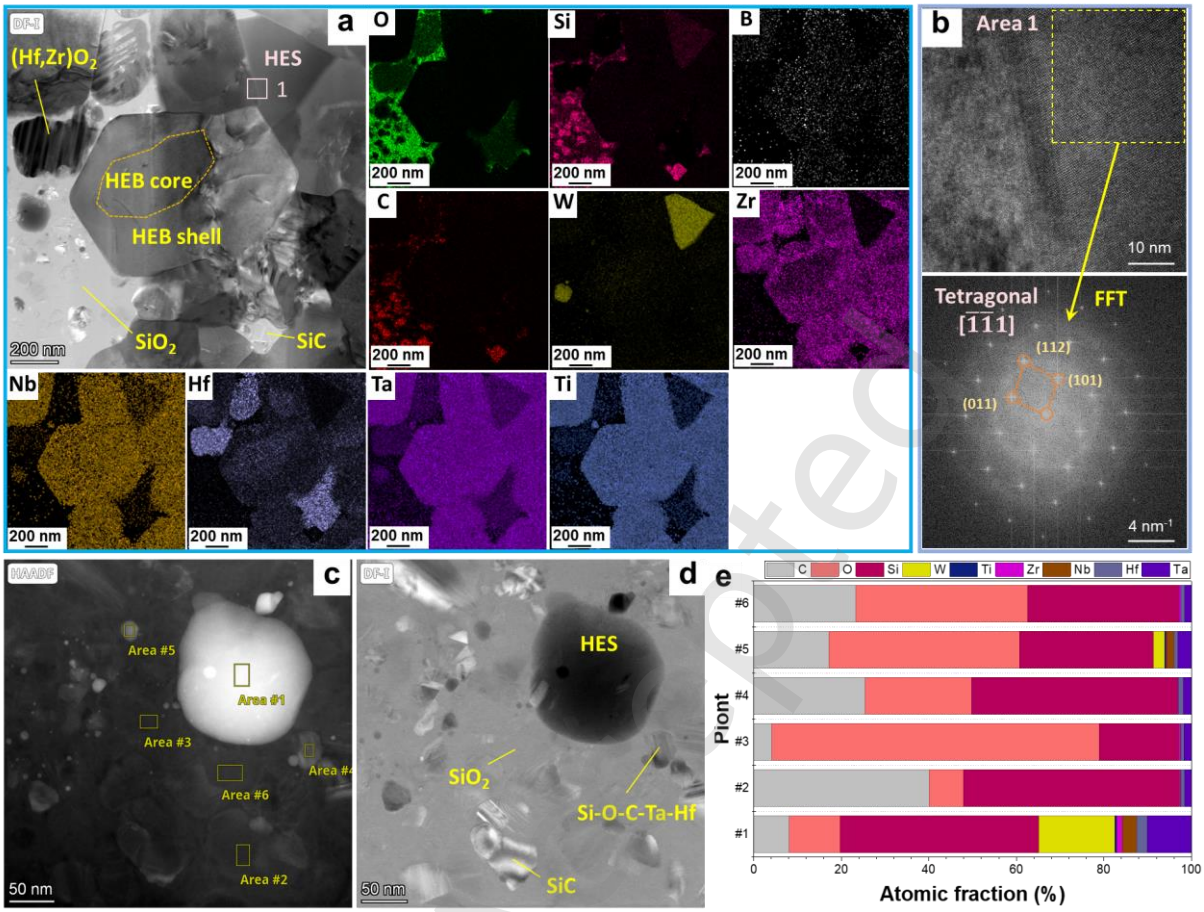

Fig. 7 (a) TEM image and EDS mappings, (b) HRTEM image of selected area marked in (a), (c) enlarged TEM image and (d) its BF image, (e) EDS spot analysis of selected area marked in (c).

Based on the above findings, Fig. 8 schematically illustrates the microstructural evolution of HEB-based ceramics during reactive $ZrSi_2$-assisted heavy direct current sintering. The use of heavy direct current-assisted sintering enabled an average heating rate of up to 1670 °C/min, allowing rapid fabrication of HEB-based ceramics. During sintering, $ZrSi_2$ likely introduced a local chemical potential gradient, driving interdiffusion or cation exchange between HEB and $ZrSi_2$. Specifically, Zr from $ZrSi_2$ diffused into the HEB matrix, while Ti, Nb, and Ta from HEB diffused into the silicide. This process resulted in the formation of a core-shell structure with a Zr-rich HEB shell. Concurrently, WC impurities introduced during ball milling reacted with $ZrSi_2$ to form SiC, while W entered the silicide

lattice. Ultimately, $(Ti_{0.04}Nb_{0.41}Ta_{0.20}W_{0.35})Si_2$ phases with a layered structure were formed.

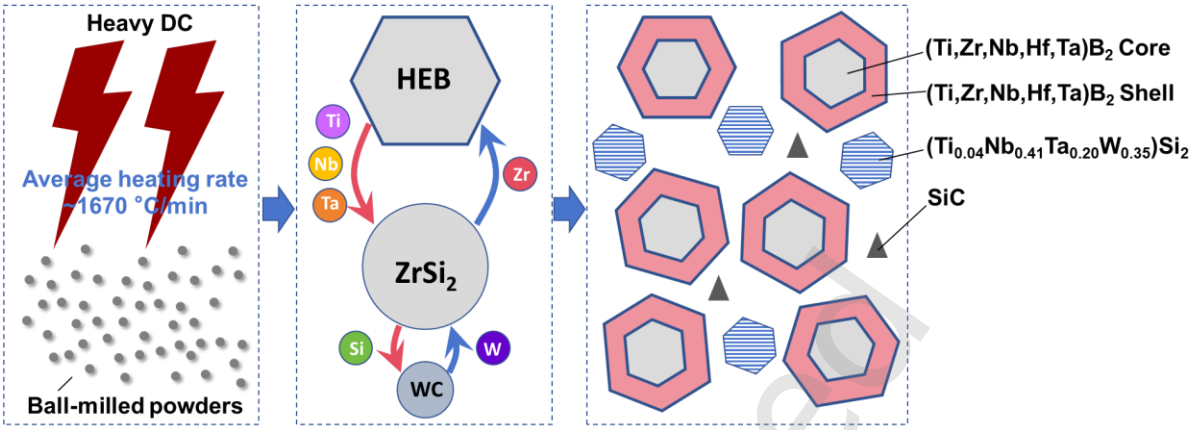

Fig.8 Schematic diagram illustrating the microstructural evolution of HEB-$ZrSi_2$ ceramics during heavy direct current-assisted sintering process

3.2. Mechanical properties and toughening mechanisms

Flexural strength and fracture toughness of the HEB-based ceramics as a function of sintering temperature are presented in Fig. 9(a). The HEB-based ceramic sintered at 1000 °C exhibits flexural strength of 760 ± 47 MPa and fracture toughness of 5.3 ± 0.1 MPa·$m^{1/2}$. With increasing temperature, the flexural strength initially rises, reaching a peak of 963 ± 33 MPa at 1400 °C, followed by a decline to 856 ± 64 MPa at 1500 °C. In terms of fracture toughness, the material maintains a value of approximately 6.6 MPa·$m^{1/2}$ across the temperature range of 1200-1400 °C, which further increases to 7.4 ± 0.1 MPa·$m^{1/2}$ at 1500 °C. A comparison with other HEB-based systems (Fig. 9(b)) shows that single-phase high-entropy boride ceramics typically exhibit flexural strengths of 339-528 MPa and fracture toughness values of 2.6-5.4 MPa·$m^{1/2}$ [14, 16, 17, 47-50]. The incorporation of secondary phases such as SiC or B_4C can increase flexural strength to ~ 750 MPa [9, 14, 16, 47, 48, 51], while the fracture toughness generally remains below 5 MPa·$m^{1/2}$. The addition of Ti_3AlC_2 has been shown to enhance toughness to 5.8 MPa·$m^{1/2}$ with a corresponding strength of 629 MPa [20]. Reinforcement with carbon fibers improves toughness through crack deflection, bridging, and pull-out, with reported

toughness up to 6.15 MPa·m$^{1/2}$ [16]. Meanwhile, the incorporation of Al_2O_3 has resulted in a toughness of 6.78 MPa·m$^{1/2}$ [19]. In comparison with these reported data, the HEB-based ceramics developed in this work exhibit superior mechanical properties, achieving an excellent combination of high flexural strength and exceptional fracture toughness at significantly reduced sintering temperatures. These results indicate that reactive $ZrSi_2$-assisted heavy direct sintering not only enables low temperature sintering but also enhances mechanical performance.

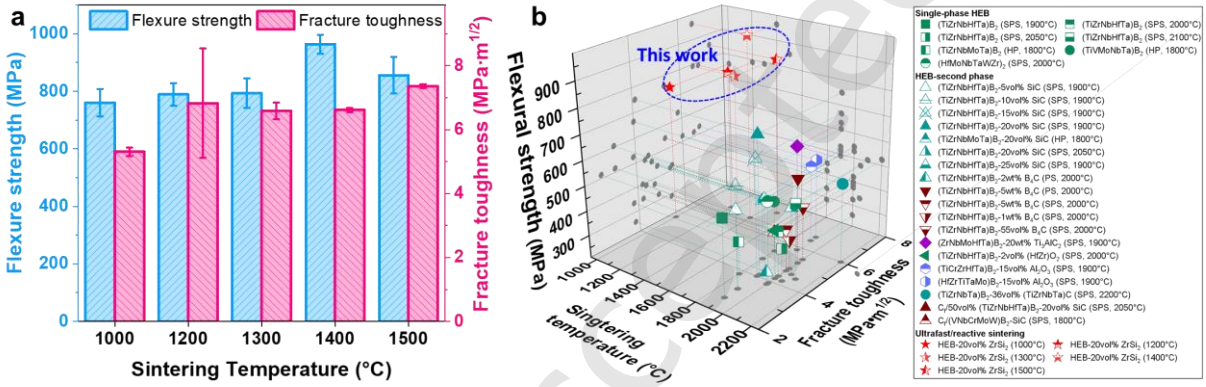

Fig.9 (a) flexural strength and fracture toughness of HEB-based ceramics sintered via reactive $ZrSi_2$-assisted direct current sintering, (b) comparison of mechanical properties with other high-entropy borides-based composite [9, 14-17, 19, 20, 41, 47-52].

Fracture morphologies of the HZ1500 are shown in Fig. 10(a)-10(h). The fracture mode is mixed intergranular and transgranular, indicating that both grain boundaries and grain interiors contribute to crack propagation. A distinct topographical contrast is observed between core and shell regions of the HEB grains (Figs. 10(b) and 10(c)), with cores appearing either recessed or elevated relative to the shell, creating a non-planar, convoluted fracture topography. This morphology reflects differences in mechanical properties or residual stresses arising from compositional gradients between the core and shell. A harder or more brittle phase tends to fracture with limited deformation, leading to height differences on the fracture plane [23]. Shell regions occasionally exhibit step-like or terraced fracture

patterns (Figs. 10(d)-10(f)), characteristic of crack deflection and bifurcation at interfaces. When a crack encounters an interface with weaker bonding or toughness mismatch, it may deviate, split, or be arrested, increasing fracture surface area and energy dissipation.

In addition to the HEB matrix, the fracture behavior of secondary phases also plays a critical role in the overall toughening response. Both the high-entropy silicide (HES) and SiC phases exhibit layered cleavage patterns (Fig. 10(g) and 10(h)), indicative of their anisotropic, plate-like structure. Fracture along weaker crystallographic planes in these phases promotes crack branching and microcracking ahead of the main crack tip, contributing to energy dissipation and toughening.

Crack propagation paths observed in the HEB-based ceramics further illustrate the toughening mechanisms (Figs. 10(i)-10(m)). Crack deflection, branching, and bridging are evident along the propagation trajectory (Figs. 10(i) and 10(j)). Cracks propagate in a zigzag manner, exhibiting a non-planar fracture mode. Near core-shell HEB grains, cracks undergo significant deflection, leading to complex trajectories and triggering the formation of secondary cracks (Figs. 10(j)-10(l)). This phenomenon substantially increases energy dissipation during crack propagation. Furthermore, branching through core-shell HEB grains (Fig. 10(m)) redistributes and weakens the local driving force at the crack tip, effectively impeding further propagation. The effectiveness of these crack-deflection mechanisms is closely tied to the evolution of the core-shell structure: as sintering temperature increases, the shell thickness grows (from 80 ± 47 nm at 1000 °C to 239 ± 188 nm at 1500 °C), which provides more pronounced interfaces for crack interaction and thereby contributes to the observed toughness enhancement (from 5.3 ± 0.1 $MPa \cdot m^{1/2}$ at 1000 °C to 7.4 ± 0.1 $MPa \cdot m^{1/2}$ at 1500 °C).

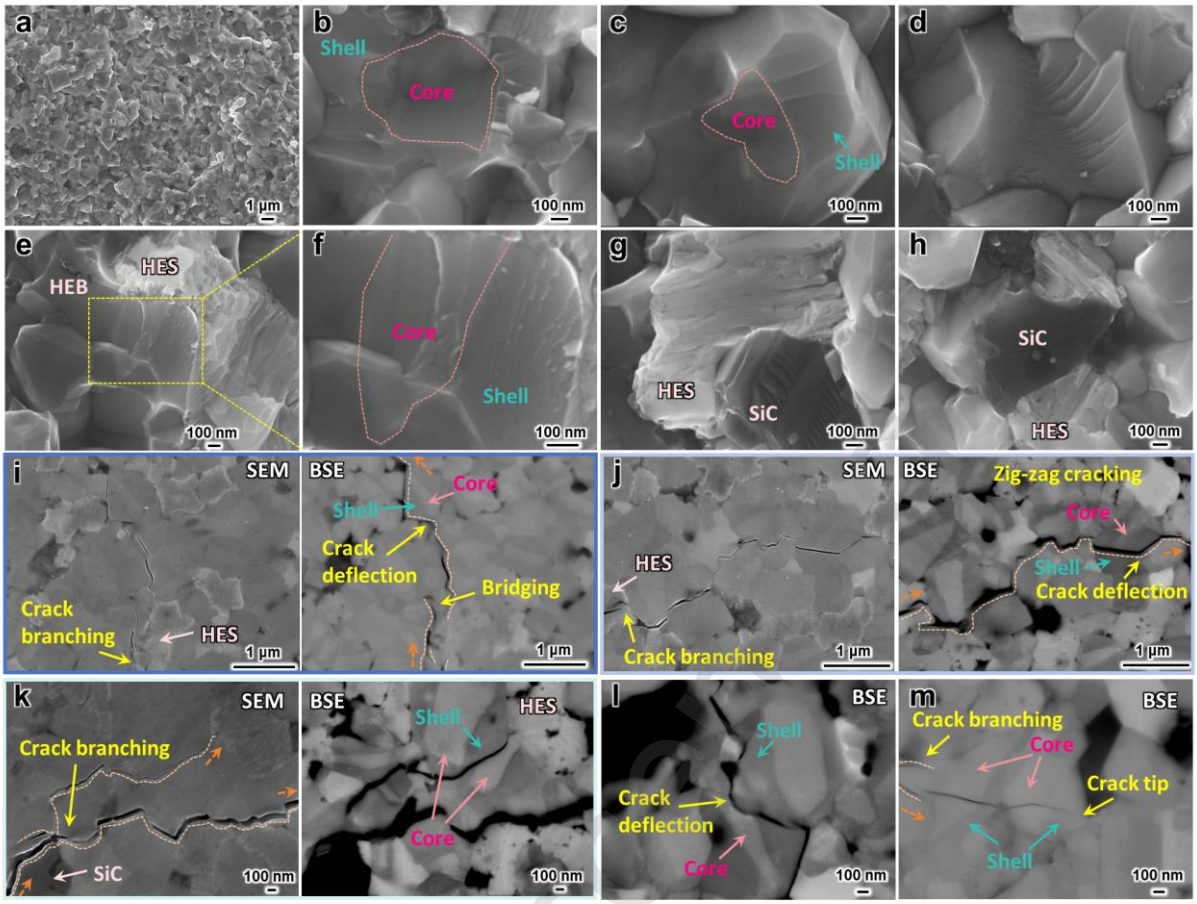

Fig. 10 (a-h) SEM images of fracture surfaces of HZ1500, (i-m) SEM images of Vickers indentation produced cracks and crack propagation paths.

To further elucidate the strengthening and toughening mechanisms within the HEB matrix, fine structures within the core-shell HEB were examined, and lattice strains were evaluated using geometric phase analysis (GPA). As shown in Figs. 11 (a)-11(c), dislocations are observed in both the core and shell regions of HEB grains, likely originating from processing-induced lattice distortions and thermal-expansion mismatch between core and shell [53]. Moreover, distinct kink-bands are also identified (Figs. 11 (d) and 11(e)). Kink-band formation acts as an energy-dissipation mechanism, involving lattice bending and rotation that absorb substantial mechanical energy [54]. When a crack encounters a kink-band, propagation is diverted and delayed. Kink bands are generally associated with activation of multiple slip systems, increasing the variety of dislocation motion and enhancing work-hardening

capability, thereby improving both strength and toughness [55].

GPA-derived in-plane strain (ε_{xx}), out-of-plane strain (ε_{yy}), and shear strain (ε_{xy}) distributions of the HEB are shown in Figs. 11 (f) and 11(g). Fig. 11 (f) shows strain distribution in a dislocation-dense region, where strain fields are clearly heterogeneous due to dislocation influence. Fig. 11 (g) presents GPA results from a core-shell HEB interface region, indicating that the shell region exhibits larger ε_{xx} strains, whereas the core region shows larger ε_{yy} strains. This heterogeneous strain field at the core-shell interface, combined with the presence of dislocations and kink bands, creates a complex local stress state that effectively hinders crack propagation and alters its path.

In summary, the enhanced mechanical properties of the HEB-based ceramics arise from the synergistic contributions of multiple microstructural features. The HEB matrix contributes through core-shell architecture and non-uniform stress fields. The secondary phases, such as HES and SiC, provide additional toughening via crack bridging, branching, and layered cleavage. The interplay between these mechanisms across different length scales results in an exceptional combination of high flexural strength and fracture toughness at significantly reduced sintering temperatures.

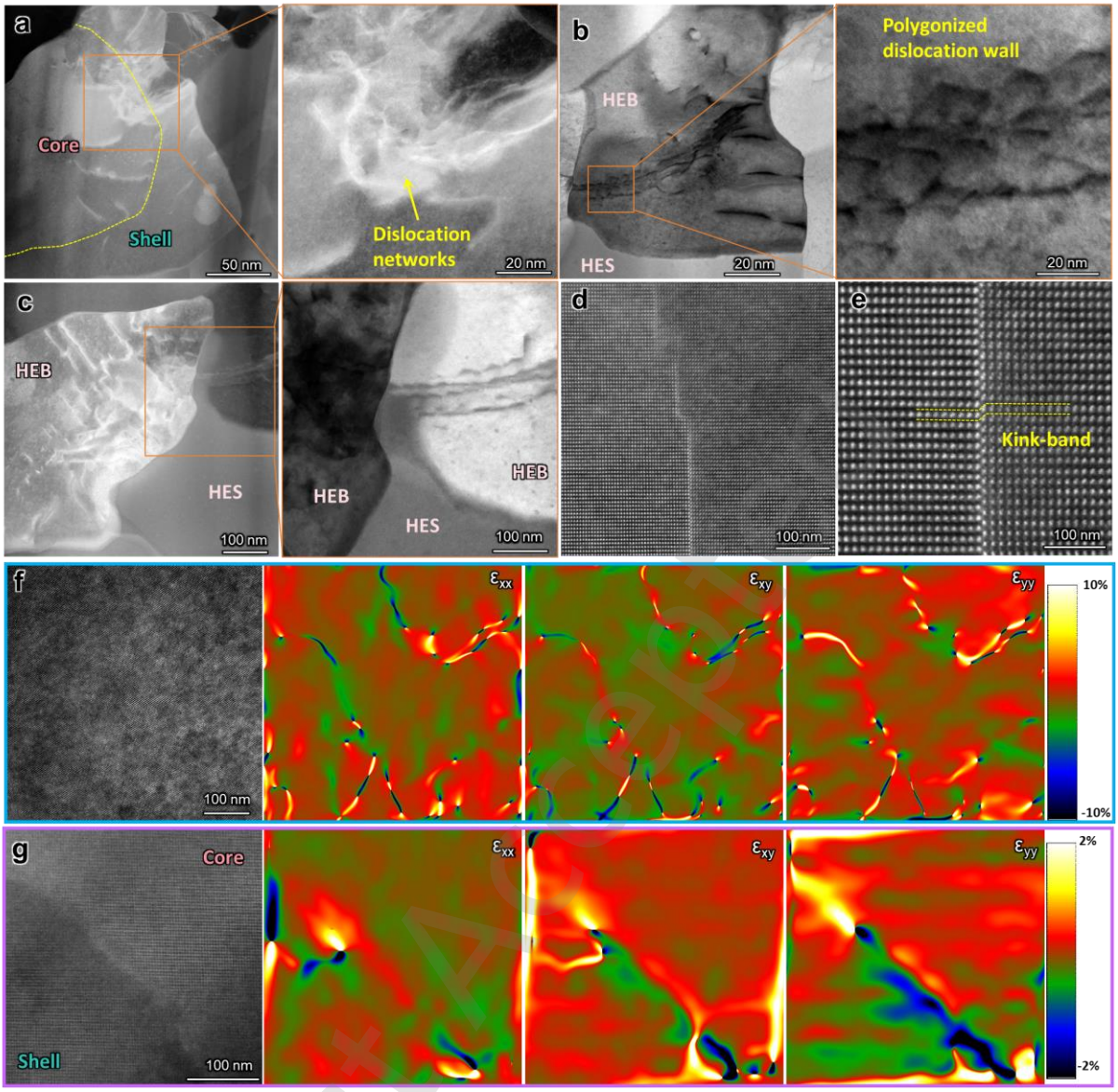

Fig. 11 (a-c) TEM images of HEB-based ceramics, showing dislocations, (d-e) STEM-HAADF images of HEB, showing kink-band, GPA analysis results from (f) high density of dislocations region and (g) the core-shell interface region.

4. Conclusion

In this study, HEB-based ceramics were fabricated via reactive $ZrSi_2$-assisted heavy direct current sintering. The main conclusions are as follows:

1) Reactive $ZrSi_2$-assisted heavy direct current sintering enables ultrafast densification of HEB-based ceramics, with a maximum heating rate exceeding 3700 °C/min. A porosity of 1.60 ± 0.61% can

be achieved at a low temperature of 1000 °C, significantly reducing the sintering temperature by 600-1000 °C compared to state-of-the-art SPS/FAST processing of HEBs.

2) Microstructural characterization confirmed interdiffusion between HEB and $ZrSi_2$ during sintering, leading to the formation of a core-shell structured HEB architecture and layered high-entropy silicides.

3) The composite sintered at 1400 °C achieved a flexural strength of 963 ± 33 MPa and a fracture toughness of 6.6 ± 0.1 $MPa \cdot m^{1/2}$, whereas sintering at 1500 °C yielded a flexural strength of 856 ± 64 MPa and a fracture toughness of 7.4 ± 0.1 $MPa \cdot m^{1/2}$. These results indicate excellent strength-toughness synergy.

4) The enhanced mechanical properties arise from the synergistic contributions of the HEB matrix and secondary phases. The HEB matrix contributes through core-shell architecture and non-uniform stress fields. The high-entropy silicide (HES) and SiC provide additional toughening via crack branching and layered cleavage.

5) Ultrafast heating may cause temperature delays and gradients. The quantitative contribution of each toughening mechanism (HEB core, HEB shell, HES, SiC) remains to be established. Future investigations combining advanced characterization with multi-scale modeling will help deconvolute these synergistic effects and further optimize the strength-toughness balance.

Acknowledgments

This work was supported by National Natural Science Foundation of China [grant number 52572320]; Natural Science Basic Research Program of Shaanxi [grant numbers 2024JC-YBQN-0580, 2025JC-YBMS-403]; Key Research and Development Program of Shaanxi [grant number 2025JC-QYCX-042]; Scientific Research Program Funded by Education Department of Shaanxi Provincial Government [grant numbers 25JP031, 25JK0379, 24JS006]; Science Foundation of Shaanxi University of Technology for Youths [grant number SLGRCQD015]; and Open Research Projects of the Shaanxi Provincial Key Laboratory of Advanced Manufacturing and Health Management for

Aviation Components [grant number SLGKFKT06].

Declaration of competing interest

The authors have no competing interests to declare that are relevant to the content of this article.

References

[1] Divilov S, Eckert H, Hicks D, et al. Disordered enthalpy-entropy descriptor for high-entropy ceramics discovery [J]. *Nature,* 2024, 625(7993): 66-73.

[2] Peters AB, Zhang D, Chen S, et al. Materials design for hypersonics [J]. *Nat Commun,* 2024, 15(1): 3328.

[3] Wang F, Monteverde F, Cui B. Will high-entropy carbides and borides be enabling materials for extreme environments? [J]. *Int J Extreme Manuf,* 2023, 5(2): 022002.

[4] Xiang H, Yan X, Dai F-Z, et al. High-entropy ceramics: Present status, challenges, and a look forward [J]. *J Adv Ceram,* 2021, 10.

[5] Qureshi T, Khan MM, Pali HS. Review: high-entropy borides-challenges and opportunities [J]. *J Mater Sci,* 2024, 59(34): 15921-15991.

[6] Nie X, Xu J, Zhang Z, et al. The progress of research on high-entropy ceramics in the field of tribology [J]. *Adv Ceram,* 2025, 46(1): 1-23.

[7] Qiu S, Zou J, Liu J, et al. Achieving superhardness and enhanced toughness in high-entropy boride-based composites by tailoring their multi-scale microstructures [J]. *Small,* 2025, 21(8): 2404632.

[8] Zhang S, Liu J, Tang H, et al. Optimized preparation and mechanical properties of high-entropy boride ceramics [J]. *Mater Today Commun,* 2025, 44: 111926.

[9] Wang F, Xu L, Zou J, et al. Pressureless densification and properties of high-entropy boride

ceramics with B_4C additions [J]. *J Mater Sci Technol,* 2024, 190: 1-9.

[10] Zhang Y, Sun S-K, Guo W-M, et al. Fabrication of textured $(Hf_{0.2}Zr_{0.2}Ta_{0.2}Cr_{0.2}Ti_{0.2})B_2$ high-entropy ceramics [J]. *J Eur Ceram Soc,* 2021, 41(1): 1015-1019.

[11] Smith SM, Fahrenholtz WG, Hilmas GE, et al. Intermediate stage densification kinetics of high-entropy ceramics during spark plasma sintering [J]. *J Eur Ceram Soc,* 2025, 45(5): 117136.

[12] Volodko S, Moskovskikh D, Kochetov N, et al. Heterogeneous microstructures in dual-phase high-entropy carbide/boride ceramics [J]. *Mater Sci Eng A,* 2025, 945: 149045.

[13] Yuan B, Guo Q, Ying H, et al. Fabrication and oxidation resistance of metallic Ta-reinforced high-entropy $(Ti,Zr,Hf,Nb,Ta)B_2$ ceramics [J]. *Materials,* 2025, 18(19): 4642.

[14] Kombamuthu V, Ünsal H, Chlup Z, et al. Effect of SiC on densification, microstructure and mechanical properties of high entropy diboride $(Ti_{0.2}Zr_{0.2}Hf_{0.2}Nb_{0.2}Ta_{0.2})B_2$ [J]. *J Eur Ceram Soc,* 2024, 44(9): 5358-5369.

[15] Liu J, Yang Q, Zou J, et al. Strong high-entropy diboride ceramics with oxide impurities at 1800°C [J]. *Sci China Mater,* 2023, 66(5): 2061-2070.

[16] Huang F, Wang H, Fang C, et al. Improved damage tolerance and oxidation resistance of $(Ti_{0.2}Zr_{0.2}Hf_{0.2}Nb_{0.2}Ta_{0.2})B_2$-SiC by introducing chopped carbon fibers [J]. *J Adv Ceram,* 2024, 13(1): 101-112.

[17] Feng L, Fahrenholtz WG, Hilmas GE, et al. Strength retention of single-phase high-entropy diboride ceramics up to 2000°C [J]. *J Am Ceram Soc,* 2024, 107(3): 1895-1904.

[18] Gao W, Wang X, Wang X, et al. Preparation of $(Ti,Zr,Hf)B_2$ powders and effect of B_4C content on the high temperature flexural strength of medium entropy ceramics [J]. *Adv Ceram,* 2023, 44(4): 342-351.

[19] Li B, Sun J, Zhang K, et al. Densification and mechanical properties of Al_2O_3 reinforced high-entropy diboride ceramics [J]. *Adv Appl Ceram,* 2025, 124: 112 - 120.

[20] Ji C, Wang H, Li M, et al. Microstructure and mechanical properties of high-entropy diboride-based ceramic assisted by Ti_3AlC_2 additive [J]. *Ceram Int,* 2024, 50(17, Part B): 30810-30820.

[21] Awin EW, Papakollu K, Vayyala A, et al. Tailoring crystal structure of high-entropy carbides in Si-based ceramic nanocomposites through precursor engineering [J]. *J Eur Ceram Soc,* 2024, 44(12): 6901-6910.

[22] Du B, Guo L, Huang Q, et al. Novel synthesis of (Hf0.25Zr0.25Ti0.25Ta0.25)C-SiC biphasic ceramic micro-powders using single-source-precursor route [J]. *Ceram Int,* 2024, 50(22, Part B): 46166-46172.

[23] Gilli N, Watts J, Fahrenholtz WG, et al. Design of ultra-high temperature ceramic nano-composites from multi-scale length microstructure approach [J]. *Compos Part B-Eng,* 2021, 226: 109344.

[24] Hao R, Zhang X, Qin J, et al. Theoretical prediction of structural stability, electronic and elastic properties of $ZrSi_2$ under pressure [J]. *RSC Adv,* 2015, 5(46): 36779-36786.

[25] Potanin AY, Zaitsev AA, Pogozhev YS, et al. Combustion synthesis of the (Ti,Zr)B_2-(Zr,Ti)C eutectic composites: Structure formation and properties [J]. *Ceram Int,* 2024, 50(22, Part B): 47433-47444.

[26] Wei B, Jiang W, Wang D, et al. Dual plate-like grains of (Ti, Zr)B2 and W2B5 toughened solid solution composites fabricated via in-situ reaction spark plasma sintering of (Ti, W)C and ZrB2 powders [J]. *J Eur Ceram Soc,* 2024, 44(11): 6206-6222.

[27] Liu D, Wen T, Ye B, et al. Synthesis of superfine high-entropy metal diboride powders [J].

Scr Mater, 2019, 167: 110-114.

[28] Liu Y, Sha J, Su C, et al. Phase composition, densification behavior and high-temperature strength of carbon-doped ZrB_2-$ZrSi_2$ ceramics [J]. *Ceram Int,* 2023, 49(23): 39083-39089.

[29] Liu Y, Liu S, Yao Y, et al. Ultrafast preparation of dense textured ZrB_2-based ceramics via heavy continuous DC Joule heating and pressing [J]. *J Adv Ceram,* 2025, 14(5): 9221074.

[30] Shen H, Zhao L, Kong X, et al. Ultrafast high-temperature sintering: Principles, advantages, and applications [J]. *J Eur Ceram Soc,* 2025, 45(16): 117653.

[31] Liu Z, He Z, Li Z, et al. Large-diameter ceramic room-temperature flash sintering technology based on new carbon electrodes [J]. *J Adv Ceram,* 2025, 14(6): 9221094.

[32] Sakkaki M, Sadegh Moghanlou F, Vajdi M, et al. Numerical simulation of heat transfer during spark plasma sintering of zirconium diboride [J]. *Ceram Int,* 2020, 46(4): 4998-5007.

[33] Biesuz M, Beauvoir THd, De Bona E, et al. Ultrafast high-temperature sintering (UHS) vs. conventional sintering of 3YSZ: Microstructure and properties [J]. *J Eur Ceram Soc,* 2024, 44(7): 4741-4750.

[34] De Bona E, Manière C, Sglavo VM, et al. Ultrafast high-temperature sintering (UHS) of ZrB_2-based materials [J]. *J Eur Ceram Soc,* 2024, 44(1): 567-573.

[35] Mao H-R, Dong E-T, Jin S-B, et al. Ultrafast high-temperature synthesis and densification of high-entropy carbides [J]. *J Eur Ceram Soc,* 2022, 42(10): 4053-4065.

[36] Zuo F, Wu R-D, Zhan L-H, et al. Scalable and efficient consolidation of Al_2O_3 and SiC ceramics using a powder medium-based ultrafast high-temperature sintering (P-UHS) [J]. *Scr Mater,* 2025, 266: 116768.

[37] Lebas F, Karacasulu L, Biesuz M, et al. Exploration of UHS scalability by SPS

approach: Multiphysics simulation, critical dimensions, mechanisms and properties [J]. *J Eur Ceram Soc,* 2026, 46(3): 117865.

[38] Gild J, Braun J, Kaufmann K, et al. A high-entropy silicide: $(Mo_{0.2}Nb_{0.2}Ta_{0.2}Ti_{0.2}W_{0.2})Si_2$ [J]. *J Materiomics,* 2019, 5(3): 337-343.

[39] Sha J, Wei Z, Li J, et al. Mechanical properties and toughening mechanism of WC-doped ZrB_2-$ZrSi_2$ ceramic composites by hot pressing [J]. *Mater Des,* 2014, 62: 199-204.

[40] Li J, Chen S, Fan H, et al. High-entropy $(Ti_{0.2}V_{0.2}Nb_{0.2}Mo_{0.2}W_{0.2})Si_2$ with excellent high-temperature wear resistance [J]. *J Am Ceram Soc,* 2024, 107(4): 2750-2764.

[41] Huang F, Wang H, Fang C, et al. Reactive sintered dense carbon fiber reinforced high-entropy boride composite using high-entropy silicide as reactant [J]. *J Am Ceram Soc,* 2024, 108(2): e20212.

[42] Qin Y, Liu J-X, Li F, et al. A high entropy silicide by reactive spark plasma sintering [J]. *J Adv Ceram,* 2019, 8(1): 148-152.

[43] Qin Y, Wang J-C, Liu J-X, et al. High-entropy silicide ceramics developed from $(TiZrNbMoW)Si_2$ formulation doped with aluminum [J]. *J Eur Ceram Soc,* 2020, 40(8): 2752-2759.

[44] Yao G, Wang W-Y, Li P-X, et al. Electronic structures and strengthening mechanisms of superhard high-entropy diborides [J]. *Rare Met,* 2023, 42(2): 614-628.

[45] Zheng Q, Gu H, Hu D, et al. Transient liquid-phase to guide multiphase evolution in reactive-hot-pressed ZrB_2-SiC-ZrC ceramics [J]. *J Materiomics,* 2020, 6(3): 607-617.

[46] Xie H, Qin M, Hong M, et al. Rapid liquid phase-assisted ultrahigh-temperature sintering of high-entropy ceramic composites [J]. *Sci Adv,* 2022, 8(27): eabn8241.

[47] Qiao L, Liu Y, Gao Y, et al. First-principles prediction, fabrication and characterization of

($Hf_{0.2}Nb_{0.2}Ta_{0.2}Ti_{0.2}Zr_{0.2}$)$B_2$ high-entropy borides [J]. *Ceram Int,* 2022, 48(12): 17234-17245.

[48] Liu J, Shen X, Wu Y, et al. Mechanical properties of hot-pressed high-entropy diboride-based ceramics [J]. *J Adv Ceram,* 2020, 9(4): 503-510.

[49] Li J, Su Y, Chen S, et al. High-entropy diboride: A novel high-temperature self-lubricating ceramic with enhanced mechanical and tribological properties [J]. *J Adv Ceram,* 2025, 14(6): 9221085.

[50] Murchie AC, Watts JL, Fahrenholtz WG, et al. Room-temperature mechanical properties of a high-entropy diboride [J]. *Int J Appl Ceram Technol,* 2022, 19(4): 2293-2299.

[51] Wang D, Xu K, Li Q, et al. Microstructure and mechanical properties of in-situ B_4C-(TiZrHfNbTa)B_2 composite by reactive spark plasma sintering [J]. *JOM,* 2022, 74(11): 4129-4137.

[52] Mao M, Huo S, Chen L, et al. A new route to fabricate dual-phase compositionally complex ceramics [J]. *J Eur Ceram Soc,* 2024, 44(15): 116726.

[53] Silvestroni L, Gilli N, Migliori A, et al. A simple route to fabricate strong boride hierarchical composites for use at ultra-high temperature [J]. *Compos Part B-Eng,* 2020, 183: 107618.

[54] Luo W, Xue T, Zuo D, et al. Formation and strengthening mechanism of kink bands in an ultra-coarse-grained Fe-Cr-Al alloy [J]. *J Mater Sci Technol,* 2024, 186: 1-14.

[55] Liu P, Hou B, Wang A, et al. Superior strength-plasticity synergy in a heterogeneous lamellar Ti_2AlC/TiAl composite with unique interfacial microstructure [J]. *J Mater Sci Technol,* 2023, 159: 21-32.